Remote Sensing Image Thresholding Methods for Determining Landslide Activity

Paul L. Rosin
School of Computer Science
Cardiff University
UK
Paul.Rosin@cs.cf.ac.uk

Javier Hervás
Institute for the Protection and Security of the Citizen
European Commission – DG Joint Research Centre
Ispra, VA
Italy
javier.hervas@jrc.it

Abstract

Detecting landslides and monitoring their activity is of great relevance for disaster prevention, preparedness and mitigation in hilly areas. To this end, change detection techniques are developed and applied to multi-temporal digital aerial photographs, simulating the very high spatial resolution of new satellite sensor optical imagery, over the Tessina complex landslide in north-eastern Italy. Several automatic thresholding algorithms are compared on the difference orthorectified and radiometrically normalised images, including some standard methods based on clustering, statistics, moments, and entropy, as well as some more novel techniques previously developed by the authors. In addition, a variety of filters are employed to eliminate much of the undesirable residual clutter in the thresholded difference image, mainly as a result of natural vegetation and man-made land cover changes. These filters are based on shape and size properties of the connected sets of pixels in the threshold maps. This has enabled us to discriminate most ground surface changes related to the movement of a preexisting landslide.

1 Introduction

Landslides constitute a major hazard to population, property and infrastructure in many hilly and mountainous areas. Detecting landslides and monitoring their activity is therefore of great relevance for disaster prevention, preparedness and mitigation. Since the advent of regularly-acquired both SAR and high spatial resolution optical imagery from space platforms, often providing also stereoscopic capability, remote sensing is increasingly used not only to assist in landslide investigations by deriving area-wide land use, geological and geomorphological information in landslide-prone areas, but also for direct delineation of landslide surface boundaries and monitoring their activity. In large scale landslide monitoring, remote sensing can still be a powerful complement to point-based ground surveying techniques (cf. (Keaton & DeGraff 1996) for a review of such techniques). Yet, traditional visual photo-interpretation methods for landslide mapping and monitoring (Soeters & van Westen 1996) should not be underestimated with the availability of latest-generation space-borne digital imagery.

Differential SAR interferometry (DInSAR) has proved capable of measuring landslide centimetric displacements (e.g. (Fruneau, Achache & Delacourt 1996, Rott, Scheuchl, Siegel & Grasemann 1999, Vietmeier, Wagner & Dikau 1999, Refice, Bovenga, Wasowski & Guerriero 2000)). However, its application may be constrained by unfavourable SAR imaging geometry with respect to slopes, inadequate spatial resolution for landslides with high internal deformation, atmospheric effects, and especially signal phase decorrelation due to both vegetation and soil moisture changes between SAR data takes. Yet fast landslides may not be resolved by time-separated SAR data acquisitions. Digital aerophotogrammetry and correlation techniques have also been successfully employed to derive surface velocity vectors of metric order on rock glaciers and rock slides in high alpine areas (Kääb 1997, Kääb 2000). This technique appears however restricted to landslides with extensive rock outcrops in the absence of major surface changes within the landslide body. The recent availability of about 1m-resolution optical imagery from the IKONOS, Quickbird and

EROS A1 satellites creates however new alternatives for landslide monitoring over extensive areas. To evaluate the potential application of these new images to detect ground surface changes as a result of major slope movements, we have developed change detection, thresholding, and shape based region filtering methods. These were applied to digitised panchromatic aerial photographs taken over the Tessina landslide in Veneto, Italy (figure 1).

The Tessina landslide affects an area including small villages, scattered houses, grassland, woodland and orchards. It has developed on Eocene flysch deposits composed of marl, sandstone and calcareous units overlaying Jurassic limestone (Pasuto, Silvano & Bozzo 1993). The movement consists of a series of rotational slides at its head quickly transforming into a 2km-long mudflow. Surficial Quaternary deposits including colluvium and glacial till have also been mobilised by the landslide. The Tessina landslide, which was first triggered in 1960, has since undergone a number of movement episodes, some of which have disrupted communication and threatened the villages of Funès and Lamosano, east of the city of Belluno. The latest major reactivation of the landslide occurred in 1992, when its surface increased from 454,000 to 500,000 m^2 (Pasuto et al. 1993, Turrini, Abu-Zeid, Semenza, Semenza & El-Naqa 1994). After this episode, the evolution of the landslide has been intensively monitored using field instrumentation (Mantovani, Pasuto, Silvano & Zannoni 2000).

Our work focused on mapping ground surface changes in the landslide body and adjacent areas as a consequence of the 1992 reactivation. Since high spatial resolution optical satellite images spanning that period were not available, we used available black and white aerial photographs of 28 September 1988, 31 August 1989 and 7 October 1994 at 1:75,000 scale. The existing high-quality photograph diapositives were precisely scanned at 14 micron to produce the 1m-resolution digital images used in this experiment.

[Insert figure 1 about here]

2 Image Pre-processing

In order to apply change detection and thresholding techniques on multi-temporal remotely sensed images, these must first be geometrically registered and radiometrically normalised. Geometrical registration of aerial photographs of hilly areas requires orthorectification of the single frames to remove relief distortions caused by central projection imaging.

To orthorectify our images, a precise 20m-grid digital elevation model (DEM) of the area was first generated from the 31 August 1989 photograph stereo pair using digital photogrammetric techniques. For this process, this epoch was used because its lower shadowing effects enabled better ground feature correlation on the photo stereo pair. This DEM resolution proved later to be adequate to produce fairly well registered orthophotographs of the Tessina area. Orthorectification was first accomplished for one of the photographs of 31 August 1989 with the help of the 20m DEM. Orthophotos were then produced from the 1988 and 1994 photographs using the same DEM and the 1989 orthophoto as reference for GCP collection. Sub-pixel accuracy was thus achieved in the orthorectification process.

The 1994 orthoimage was then radiometrically normalised to the 1988 orthoimage by applying gain and bias coefficients derived from regression analysis between the two images using pixel values taken from pseudo-invariant targets (Hall, Strebel, Nickenson & Goetz 1991, Hill & Sturm 1991). Radiometric normalisation was required to remove pixel value differences due to varying illumination, shadowing and atmospheric conditions, as well as to different camera and film response. These two images had been selected for our change detection analysis since their dates were more similar in relation to illumination effects and vegetation phenology.

3 Change Detection

After pre-processing the images are differenced. This is the most widely used method for change detection, and is both simple and relatively effective compared to more sophisticated approaches such as principal component analysis, change vector analysis (Singh 1989), and multifractal analysis (Canus & Véhel 1996). (See also (Yuan & Elvidge 1998) for extensive experimentation with change detection methods.) In addition we also consider some alternative methods for change detection based on more global properties of the two images, which will be described later.

4 Thresholding Techniques

Having created the difference image it is generally required to threshold it into two classes to provide a 'change' and 'no-change' classification. Over the years many methods have been developed for image thresholding (e.g. see (Sahoo, Soltani, Wong & Chen 1988)), but few are directly applicable for change detection in natural or semi-natural landscapes in remote sensing images, since they generally make assumptions that do not hold true in that context. For instance, many require the distribution of difference image intensities to be bimodal, and furthermore, the size of the modes should not differ too greatly. However, even in situations where two underlying classes exist, when one is much larger than the other, its contribution to the histogram is so great that it tends to swamp and effectively obliterate the presence of the other class, leaving a unimodal distribution. This has led to the recent development of several thresholding algorithms designed to operate under such conditions (Rosin 2002). These are briefly described below.

4.1 Normal and LMedS Methods

In many instances it is reasonable to assume that the image noise can be modelled by a zero mean Normal distribution $N(0, \sigma^2)$. In this case, analysing the difference in intensity images is straightforward. Differencing followed by taking the absolute value will produce the Normal distribution $2N(0, 2\sigma^2)$ for positive values only. When thresholding at $x\sigma$ the probability of incorrectly classifying a pixel as change is

$$P_F = \text{erfc}\left(\frac{x}{\sqrt{2}\sigma}\right).$$

This enables us to choose a suitable threshold τ for a given acceptable proportion of false change pixels.

In practice the variance of the noise is often unknown and so it needs to be estimated from the image. This can be done from the data in the standard fashion. Alternatively, we have used the more robust Least Median of Squares (LMedS) method which is insensitive to large amounts of outliers while remaining computationally efficient.

4.2 Poisson Method

If we assume that the noise is white then its spatial distribution over the image will be random. For the analysis of spatial data there are many measures of randomness (Upton & Fingleton 1985), often based on the assumption that the observations follow a Poisson distribution. Since a Poisson distribution has its mean equal to its variance then the ratio of the sample variance to the sample mean is a natural test for that distribution, and is called the *relative variance*

$$V_r = \frac{s^2}{\bar{x}}.$$

It is calculated by first counting the number of observations (in our case the number of above threshold pixels in the difference map) in n windows, $x_{i=1\ldots n}$, from which the mean, $\bar{x}$, and variance, s^2, of the x_i can be found. Although the test is sensitive to the window size and point density it works adequately as long as $\bar{x}$ is sufficiently large (e.g. $\bar{x} > 1$).

For mapping scene changes due to landsliding we do not wish to detect the spatially random noise, but rather to avoid it in our thresholded image. This is achieved when there is more clustering than a Poisson distribution, and is signalled by $V_r > 1$. We therefore select the threshold which maximises the relative variance, thereby maximising 'clumpiness' (regions of change) and minimising the Poisson distribution (noise).

4.3 Corner Method

A simple thresholding technique was introduced by Rosin (2001). It analyses the image histogram and selects as a threshold value the 'corner' of the curve. This is detected as the point on the curve with maximum deviation from the straight line drawn between the end points of the curve (figure 2). The assumption is that the histogram is primarily unimodal, consisting (in the context of change detection) of a main peak formed by a large set of pixels corresponding

to low levels of change, and a long tail formed by a mixture of processes such as noise, radiometric differences, and pixels corresponding to significant change. The 'corner' of the curve is an appropriate threshold since it separates the peak from the tail.

The method has been analysed and demonstrated extensively in (Rosin 2001) where it is shown to work well for a variety of thresholding tasks, including also landslide monitoring (Hervás, Barredo, Rosin, Pasuto, Mantovani & Silvano 2003). The technique is robust – it can still operate reliably even when the corner is not distinct (e.g. sharp) or the histogram is noisy – and does not depend on the histogram containing a specific (e.g. Normal, Rayleigh, etc.) distribution.

[Insert figure 2 about here]

4.4 Connectivity Method

The location, size, and number of the regions of change are generally unknown. However, we might expect that these properties will remain fairly stable over a wide range of threshold values. This is in contrast to regions occurring in the thresholded difference map due to noise; down at the noise level small changes in the threshold value can substantially alter the number of regions. Such an observation suggests that if a range of threshold values is found that leads to a stable number of regions, then these regions are unlikely to come from noise, and so a value from this range will provide a suitable threshold. This approach was suggested by O'Gorman (O'Gorman 1994) for intensity image thresholding. Rather than counting the number of regions the image's Euler number can be used, and was found to give almost identical results at much lower computational cost.

The shape of the histogram of Euler number/threshold is modelled as a decaying exponential, and a suitable partition point between the signal and noise is the 'corner' of the curve detected using the corner method described above.

5 Alternative Change Detection

When there is an appreciable time difference between the two remotely sensed images being compared it is often the case that, in addition to land cover changes (including those due to landsliding in our area), there are some systematic differences between the images. Although the radiometric normalisation should greatly reduce the effects, some residual intensity variations may remain. Additive variations have also been observed because of slight misregistration between the images in some sectors after orthocorrection. Therefore, as an alternative to simple image differencing there are various approaches to change detection that can be taken in an attempt to overcome such problems, using measures such as correlation, mutual information, etc. (Rosin 1994).

5.1 Scatter Plot Method

Another approach to attempt to identify systematic variations is to examine the mapping of intensities between the two images. A scatter plot is generated, where the point co-ordinates are the corresponding pixel intensities in the two images. Ideally this plot should show a thin straight line at $45°$, but in practise there is often some thickening and distortion. The proposed method robustly finds the central axis of the scatter plot line by calculating the LMedS estimate of the values within each row. Also at each row the median absolute deviation (MAD), which is a robust estimate of the standard deviation, is calculated. The outer acceptable boundaries in the scatter plot are then taken as the LMedS estimate $\pm 3 \times$ MAD, since the majority of the no-change population should lie in that range. Change detection is performed by labelling all pixels as change if they lie outside the scatter plot boundaries.

6 Experimental Results

Figure 3a&b shows pre-processed images of the Tessina landslide area covering the period before and after the most recent major landslide reactivation. The landslide runs from near the top right corner to the centre bottom left of the images; the thinner sector represents the mudflow. The image size is 2700×2600. The difference image (figure 3c;

black indicates high change, white no change) is calculated by taking the absolute difference of the pixel intensity values over the two dates. Examination of the histogram of the difference image shows it to be close to a folded Normal (figure 3d). The irregularity close to zero may be an artifact of incomplete radiometric normalisation or geometric registration. In figure 3e the scatter plot shows considerable spread, indicating that despite normalisation there remain appreciable differences which will complicate the thresholding process.

[Insert figure 3 about here]

To enable quantitative assessment of the accuracy of the resulting thresholded difference images reference data was extracted using on-site photographs and aerial photographs. Since we are trying to detect change we can describe the results of classification as true and false instances of change and no change as shown in table 1. We define overall accuracy (percentage correct classification) as $(TP+TN)/N$, where the number of pixels $N = TP+FP+FN+TN$. The definitions for producer's and user's accuracies for change and no change are shown in table 2.

[Insert table 1 about here]

[Insert table 2 about here]

Unfortunately, the process of quantitative evaluation is problematic (Congalton & Green 1999). In particular for the case encountered here where there are only two classes of unequal size an arbitrarily good classification of one class can be achieved at the expense of the other class. Moreover, given the lower number of true change pixels a good overall classification accuracy can still be gained at excessively high threshold values since the majority of pixels (which are from the no change class) will still be correctly classified. These problems are demonstrated in the graph in figure 4 which shows the various assessment criteria for all possible threshold values. We have found that a more useful criterion is to use the minimum of the four producer and user accuracy values, thereby penalising thresholds which perform poorly according to any of the four producer/user criteria. This gives a well defined peak (whereas the other curves tend to be monotonic), and it can be seen from figure 5 that thresholding at that value gives a good trade-off in detecting most areas of change while minimising spurious change labels.

[Insert figure 4 about here]

[Insert figure 5 about here]

Figure 6 shows the effects of applying the thresholding methods described in section 4 to the difference image. In addition, four standard image thresholding methods which cover a wide range of the available techniques are applied. These are based on clustering (Ridler & Calvard 1978), statistics (Otsu 1979), moments (Tsai 1985), and entropy (Kapur, Sahoo & Wong 1985). Changes detected by the corner, moments, Normal, LMedS and Poisson algorithms include on the one hand those within the landslide body surface as a result of the 1992 movement (for instance new soil outcrops because of disruption of the vegetation cover) and those produced after the movement on stable sectors of the landslide prior to the date of the second image. The latter represent vegetation growth together with local soil moisture increase during the relative stability period following the 1992 reactivation. These findings are confirmed by interpretation of both on-site photographs and oblique aerial photographs taken by researchers of IRPI-CNR, Padua, Italy, during the 1992 movement period, and are in agreement with reports in (Pasuto et al. 1993) and (Turrini et al. 1994). The changes detected by these five methods outside the landslide body correspond mainly to man-made changes which include changes on grass parcels, orchards, new roads, tracks, and houses, as well as tree canopy changes on woodland areas. Much of the noise is due to the residual effects after radiometric normalisation which are more severe in woodland areas. The clustering, statistical and especially the connectivity methods have overestimated the changes, while the entropy method has underestimated the changes.

[Insert figure 6 about here]

Figure 7a shows the scatter plot with the detected central axis and the threshold boundaries superimposed, resulting in the thresholded image in figure 7b. For the Tessina area, this method enhances soil freshness due to vegetation cover disruption and soil remobilisation as a result of landsliding, while still showing some noise as in the other thresholding methods.

[Insert figure 7 about here]

The numerical scores in table 3 corroborate the above conclusions. Ranking the thresholding methods by the minimum of the producer/user accuracies the corner, Poisson and LMedS perform best, closely followed by the Normal and moments methods. The remainder achieve significantly lower scores.

[Insert table 3 about here]

6.1 Blob Filtering

It is evident that simple thresholding is not sufficient to identify the true changes from the difference image. We therefore considered improving the raw thresholded output by filtering out the undesirable change blobs. This can be done based on the local properties of the blobs; we consider the following: size (area) and shape (width, perimeter and rectangularity).

In addition, more global properties also play a role, and we take into account the spatial relationships between blobs (density). The following sections describe the implementation of these filters and show their application to the thresholded image obtained from the corner method (see figure 6e).

[Insert figure 8 about here]

6.1.1 Width and Density

To eliminate blobs according to their width the well-known erosion and dilation operators are used. Applying n iterations of erosion followed by n dilations will eliminate blobs whose width is less than $2n$. To encourage grouping of fragmented blobs, i.e. the merging of pixels in dense areas, the same process can be run in reverse. Thus the results shown in figure 8a&b are generated by the sequence of n dilations, $2n$ erosions, n dilations. From the figures it can be seen that small amounts of filtering are sufficient to remove small noise blobs as well as thin structures such as paths/roads. Higher levels of filtering successfully connect the fragmented blobs within the landslide body to form a few unified regions of change. The drawback is that the man-made and vegetation changes away from the landslide are amplified.

6.1.2 Perimeter

Unlike the previous filter step, calculating the perimeter of the blobs requires the blobs to be isolated, which is carried out using connected component labelling. (Unfortunately the boundaries of objects and holes that we obtain are not distinguished, and so this causes some minor artifacts in the processing.) The perimeter filter was applied to figure 6e with two perimeter thresholds set to produce similar numbers of blobs as the width filtering. Figure 8c&d shows that narrow man-made features like new roads and tracks are better retained compared to width filtering, although for this application that is actually a disadvantage. At higher levels of filtering most of the landslide-related changes are retained while removing much of the extraneous changes.

6.1.3 Area

Having isolated the blobs their area can be easily calculated, and again appropriate thresholds are set to keep similar numbers of blobs as before. It can be seen from figure 8e&f that both the area and perimeter methods produce very similar results. Most of the changes outside the landslide have been removed and the major regions of change have been discriminated although their boundaries are coarsely delineated. Nevertheless, overall width filtering was more successful. Of course, combinations of filters can be applied in order to capitalise on their individual merits. Although the high level of width filtering in figure 8b created undesirable large noise blobs these can be removed by an area filter as shown in figure 8g, in which the true regions of change within the landslide have been fairly well discriminated, although the overall boundaries have been very coarsely delineated.

6.1.4 Rectangularity

A standard method for estimating the rectangularity of a region is applied, namely the ratio of the region's area against the area of its minimum bounding rectangle (MBR). The MBR can be efficiently calculated using Toussaint's optimal, linear algorithm (Toussaint 1983). Although the MBR is potentially sensitive to noise a comparison against some alternative algorithms for measuring rectangularity showed it to work relatively well (Rosin 1999).

Many of the man-made changes have simple polygonal shapes such as rectangular buildings, agricultural fields, and even some road segments. In some cases it would be useful to apply filtering to identify these objects. In this case however, we just wish to eliminate them since they do not typically correspond to effects of the landslide. The

effects of rejecting and retaining blobs according to their measured rectangularity in combination with perimeter and area filtering are shown in figure 9. First the perimeter or area filtering was applied. Then a suitable rectangularity threshold was selected by analysing the graph of the cumulative number of blobs retained after filtering against the threshold value, see figure 10. The rectangularity of most blobs is near the middle of the range. Since only a relatively small number of highly rectangular blobs are expected the upper bend at high rectangularity values is a suitable threshold as this occurs at the point just above the rectangularity values of the majority of the change blobs. The corner finding approach previously described for threshold selection was applied, and produced the value 0.6 which is used for all these examples. In all cases rectangularity has successfully identified most man-made changes.

When low levels of perimeter and area filtering were applied it appears that many small regions are classified as being highly rectangular. This can be explained by the fact that image discretisation imposes a restriction on the range of possible shapes at that scale, and the rectilinear grid often results in small blobs appearing rectangle like.

[Insert figure 9 about here]

[Insert figure 10 about here]

Referring to the lower section of table 3 the scores indicate that in terms of post-processing, applying large amounts of width and area filtering was most effective. According to the table rectangularity filtering was ineffectual. However, this is because the assessment values do not reflect its ability to highlight specific regions of man-made change.

7 Conclusions and Future Work

The application of thresholding methods to difference images derived from multi-temporal digital aerial photographs simulating the high spatial resolution of new satellite sensor imagery has proved useful to map ground surface changes related to landslide activity.

Of course, there are many other techniques available for change detection (Singh 1989) which we were unable to evaluate in this paper and there is still considerable active research in this field (Bruzzone & Prieto 2000). Likewise, there is much interesting work in thresholding that combines some aspects of filtering. For instance there is the soft morphology approach (Stringa 2000) and hysteresis based thresholding (Rosin & Ellis 1995).

Some constraints to this method were however found in our imagery that are mainly due to the single-band wide spectral range of aerial photographs, lack of image calibration, and especially to possible man-made and natural changes occurring during the long time elapsed between the available photos. The latter, in particular, may mask actual movement in some landslide sectors. This can however be partly overcome by making assumptions based on image analysis and field checking.

Because of the repetitive observations starting to be provided by high spatial resolution satellite sensors with multi-spectral imaging capabilities, the methods reported in this paper could become complementary to ground surveying and visual photointerpretation techniques for landslide monitoring on extensive areas at scales up to 1:5000, especially in densely vegetated areas where DInSAR techniques are often of limited application. Yet these methods can be applied to archived digital aerial photographs to determine the recent history of landslide activity at even larger scales.

Figure 11 illustrates that splitting up positive and negative change to further discriminate changes associated with landslide reactivation is part of our current research (Hervás & Rosin 2001, Hervás et al. 2003). For instance, white within the landslide body (positive change) indicates ground change patterns mostly associated with the reactivation occurred in 1992, whereas pixels in black (negative change) appear mostly associated with either simple land cover changes or soil moisture increase. The land cover changes within the landslide body are mainly related to vegetation growth, thus meaning ground stability. Widespread soil moisture increase within the landslide may be a forerunner of possible future movement. A major research effort, however, will still be needed to derive landslide movement rates from optical satellite imagery.

[Insert figure 11 about here]

Acknowledgements

This work has been partly funded by the European Commission's Research DG, under Framework Programme IV, Environment and Climate, Natural Risks (A. Ghazi, head of unit; M. Yeroyanni, scientific officer) within the RUNOUT project. The authors would like to thank José I. Barredo and Peter Spruyt of Joint Research Centre for their help in pre-processing the data. Thanks are also due to Alessandro Pasuto and Sandro Silvano, of IRPI-CNR, Padua, Italy, and Franco Mantovani, of University of Ferrara, Italy, for providing ground data.

References

Bruzzone, L. & Prieto, D. F. (2000), 'Automatic analysis of the difference image for unsupervised change detection', *IEEE Transactions on Geoscience and Remote Sensing* **38**(3), 1171–1182.

Canus, C. & Véhel, J. L. (1996), Change detection in sequences of images by multifractal analysis, *in* 'Proc. ICASSP', pp. 2178–2181.

Congalton, R. & Green, K. (1999), *Assessing the accuracy of remotely sensed data: principles and practices*, Lewis Publications.

Fruneau, F., Achache, J. & Delacourt, C. (1996), 'Observation and modelling of the Sant-Etienne-de-Tinée landslide using SAR interferometry', *Tectonophysics* **265**, 181–190.

Hall, F., Strebel, D., Nickenson, E. & Goetz, S. (1991), 'Radiometric rectification: toward a common radiometric response among multidate multisensor images', *Remote Sensing of Environment* **35**, 11–27.

Hervás, J., Barredo, J., Rosin, P., Pasuto, A., Mantovani, F. & Silvano, S. (2003), 'Monitoring landslides from optical remotely sensed imagery: the case history of Tessina landslide, Italy', *Geomorphology* **54**, 63–75.

Hervás, J. & Rosin, P. (2001), Tratamiento digital de imágenes de teledetección en el espectro óptico para el reconocimiento y control de deslizamientos, *in* 'Proceedings V Simposio Nacional sobre Taludes y Laderas Inestables', CEDEX: Madrid, pp. 63–74.

Hill, J. & Sturm, B. (1991), 'Radiometric correction of multitemporal Thematic Mapper data for use in agricultural land-cover classification and vegetation monitoring', *Int. J. Remote Sensing* **12**, 1471–1491.

Kääb, A. (1997), 'Analysing the creep of mountain permafrost using high precision aerial photogrammetry: 25 years of monitoring gruben rock glacier, Swiss Alps', *Permafrost and Periglacial Processes* **8**, 409–426.

Kääb, A. (2000), 'Photogrammetry for early recognition of high mountain hazards: new techniques and applications', *Physics and Chemistry of The Earth* **25**(9), 765–770.

Kapur, J., Sahoo, P. & Wong, A. (1985), 'A new method for gray-level picture thresholding using the entropy of the histogram', *Computer Vision, Graphics and Image Processing* **29**(3), 273–285.

Keaton, J. & DeGraff, J. (1996), Surface observation and geologic mapping, *in* K. Turner & R. Schuster, eds, 'Landslides Investigation and Mitigation', Transportation Research Board Special Report 247, National Academy Press, Washington DC, pp. 178–230.

Mantovani, F., Pasuto, A., Silvano, S. & Zannoni, A. (2000), 'Data collection aiming at the definition of future hazard scenarios of the Tessina landslide', *International Journal of Applied Earth Observation and Geoinformation* **2**(1), 33–40.

O'Gorman, L. (1994), 'Binarization and multithresholding of document images using connectivity', *CVGIP: Graphical Models and Image Processing* **56**(6), 494–506.

Otsu, N. (1979), 'A threshold selection method from gray-level histograms', *IEEE Transactions on Systems, Man and Cybernetics* **9**, 62–66.

Pasuto, A., Silvano, S. & Bozzo, G. (1993), The Tessina landslide (Belluno, Italy), *in* M. Panizza, M. Soldati & D. Barani, eds, 'First European Intensive Course on Applied Geomorphology', Istituto di Geologia, Universtità degli Studi di Modena, Italy, pp. 63–69.

Refice, A., Bovenga, F., Wasowski, J. & Guerriero, L. (2000), Use of InSAR data for landslide monitoring: a case study from southern Italy, *in* 'Proc. IGARRS'2000'.

Ridler, T. & Calvard, S. (1978), 'Picture thresholding using an iterative selection method', *IEEE Transactions on Systems, Man and Cybernetics* **8**, 629–632.

Rosin, P. (1994), Parcel-based change detection, *in* 'Image and Signal Processing for Remote Sensing', Vol. SPIE 2315, pp. 289–298.

Rosin, P. (1999), 'Measuring rectangularity', *Machine Vision and Applications* **11**, 191–196.

Rosin, P. (2001), 'Unimodal thresholding', *Pattern Recognition* **34**(11), 2083–2096.

Rosin, P. (2002), 'Thresholding for change detection', *Computer Vision and Image Understanding* **86**(2), 79–95.

Rosin, P. & Ellis, T. (1995), Image difference threshold strategies and shadow detection, *in* 'British Machine Vision Conf.', pp. 347–356.

Rott, H., Scheuchl, B., Siegel, A. & Grasemann, B. (1999), 'Monitoring very slow slope movements by means of SAR interferometry: A case study from a mass waste above a reservoir in the Otzal Alps, Austria', *Geophysics Research Letters* **26**, 1629–1632.

Sahoo, P., Soltani, S., Wong, A. & Chen, Y. (1988), 'A survey of thresholding techniques', *Computer Vision, Graphics and Image Processing* **41**, 233–260.

Singh, A. (1989), 'Digital change detection techniques using remotely sensed data', *Int. J. Remote Sensing* pp. 989–1003.

Soeters, R. & van Westen, C. (1996), Slope instability recognition, analysis and zonation, *in* K. Turner & R. Schuster, eds, 'Landslides Investigation and Mitigation', Transportation Research Board Special Report 247, National Academy Press, Washington DC, pp. 129–177.

Stringa, E. (2000), Morphological change detection algorithms for surveillance applications, *in* 'British Machine Vision Conf.', pp. 402–411.

Toussaint, G. (1983), Solving geometric problems with the rotating calipers, *in* 'IEEE MELECON '83', pp. A10.02/1–4.

Tsai, W. (1985), 'Moment-preserving thresholding', *Computer Vision, Graphics and Image Processing* **29**, 377–393.

Turrini, M., Abu-Zeid, N., Semenza, E., Semenza, P. & El-Naqa, A. (1994), New studies on the Tessina landslide, *in* '7th International IAEG Congress', pp. 1667–1675.

Upton, G. & Fingleton, B. (1985), *Spatial Data Analysis by Example, Volume 1, Point Pattern and Quantitative Data*, Wiley.

Vietmeier, J., Wagner, W. & Dikau, R. (1999), Monitoring moderate slope movements (landslides) in the southern French Alps using differential SAR interferometry, *in* '2nd Int. Workshop on ERS SAR Interferometry "FRINGE'99"'.

Yuan, D. & Elvidge, C. (1998), 'NALC land cover change detection pilot study: Washington D.C. area experiments', *Remote Sensing of the Environment* **66**(2), 166–178.

		REFERENCE CLASS	
		change	**no change**
ASSIGNED CLASS	**change**	true positive (TP)	false positive (FP)
	no change	false negative (FN)	true negative (TN)

Table 1: Labelling of all possible correct and incorrect pixel classifications.

	producer's accuracy	**user's accuracy**
change	TP/(TP+FN)	TP/(TP+FP)
no change	TN/(FP+TN)	TN/(FN+TN)

Table 2: Calculation of producer and user accuracies.

	Overall Accuracy	Minimum of Producer & User Values	Producer's Accuracy		User's Accuracy	
			Change	No Change	Change	No Change
corner	91.5	**34.54**	36.4	95.3	34.5	95.6
Poisson	91.2	**33.49**	38.0	94.8	33.5	95.7
LMedS	91.2	**33.49**	38.0	94.8	33.5	95.7
Normal	90.0	**30.16**	43.1	93.2	30.2	96.0
moments	88.9	**27.94**	46.7	91.8	27.9	96.2
statistical	84.6	**22.12**	55.9	86.6	22.1	96.6
scatter plot	91.0	**19.85**	19.8	95.9	24.7	94.6
clustering	80.5	**18.77**	61.7	81.8	18.8	96.9
entropy	93.6	**11.42**	11.4	99.3	51.4	94.3
connectivity	50.2	**9.75**	82.2	48.0	9.7	97.5
figure 8g	93.3	**48.48**	81.5	94.1	48.5	98.7
figure 8a	92.7	**42.93**	43.5	96.1	42.9	96.1
figure 8c	92.8	**33.83**	33.8	96.9	42.5	95.5
figure 8e	92.9	**33.80**	33.8	96.9	42.8	95.5
figure 9a	93.5	**32.40**	32.4	97.7	48.6	95.5
figure 8d	94.0	**31.08**	31.1	98.3	55.1	95.4
figure 8f	94.0	**30.88**	30.9	98.3	55.0	95.4
figure 9c	94.2	**30.70**	30.7	98.5	58.5	95.4
figure 8b	85.9	**28.98**	83.0	86.1	29.0	98.7
figure 9e	94.1	**27.44**	27.4	98.6	57.8	95.2
figure 9g	94.4	**26.34**	26.3	99.0	64.2	95.2

Table 3: Assessment of the threshold techniques demonstrated in figures 6 and 7 are given in the upper section. The lower section contains results of applying post-processing in the form of filtering the results from the corner algorithm; see figures 8 and 9. Entries are ordered by the minimum of the four producer/user accuracy values.

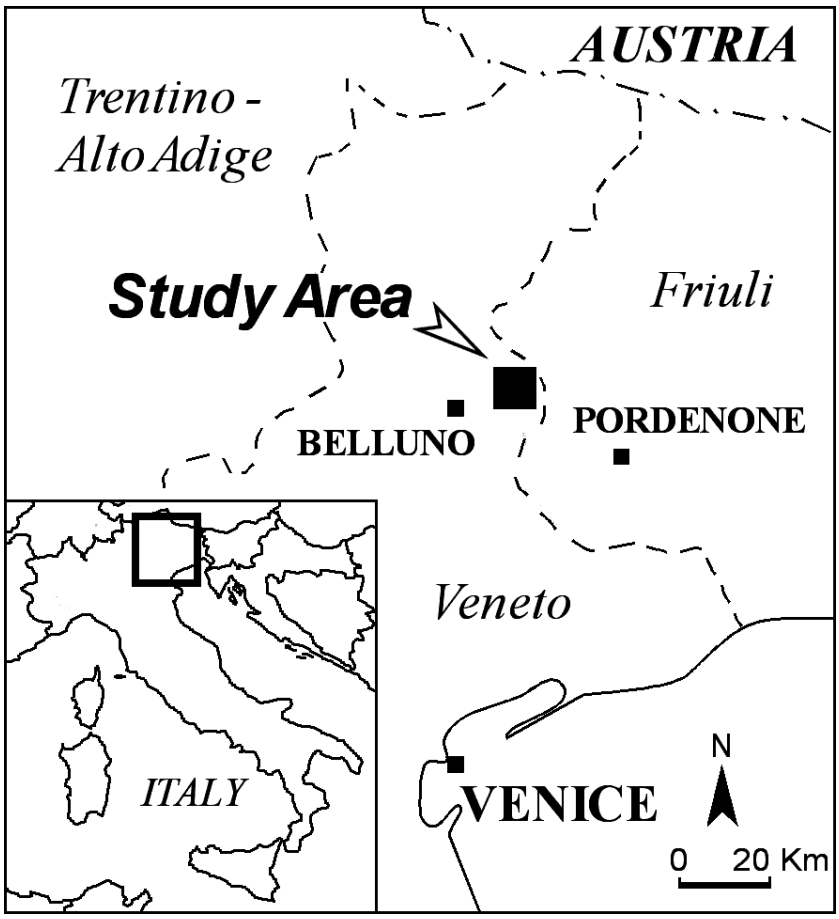

Figure 1: Location of the Tessina area

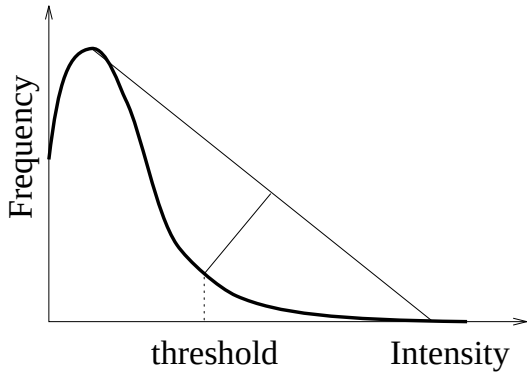

Figure 2: Determining the threshold from the histogram by locating the corner at the point of maximum deviation from the straight line

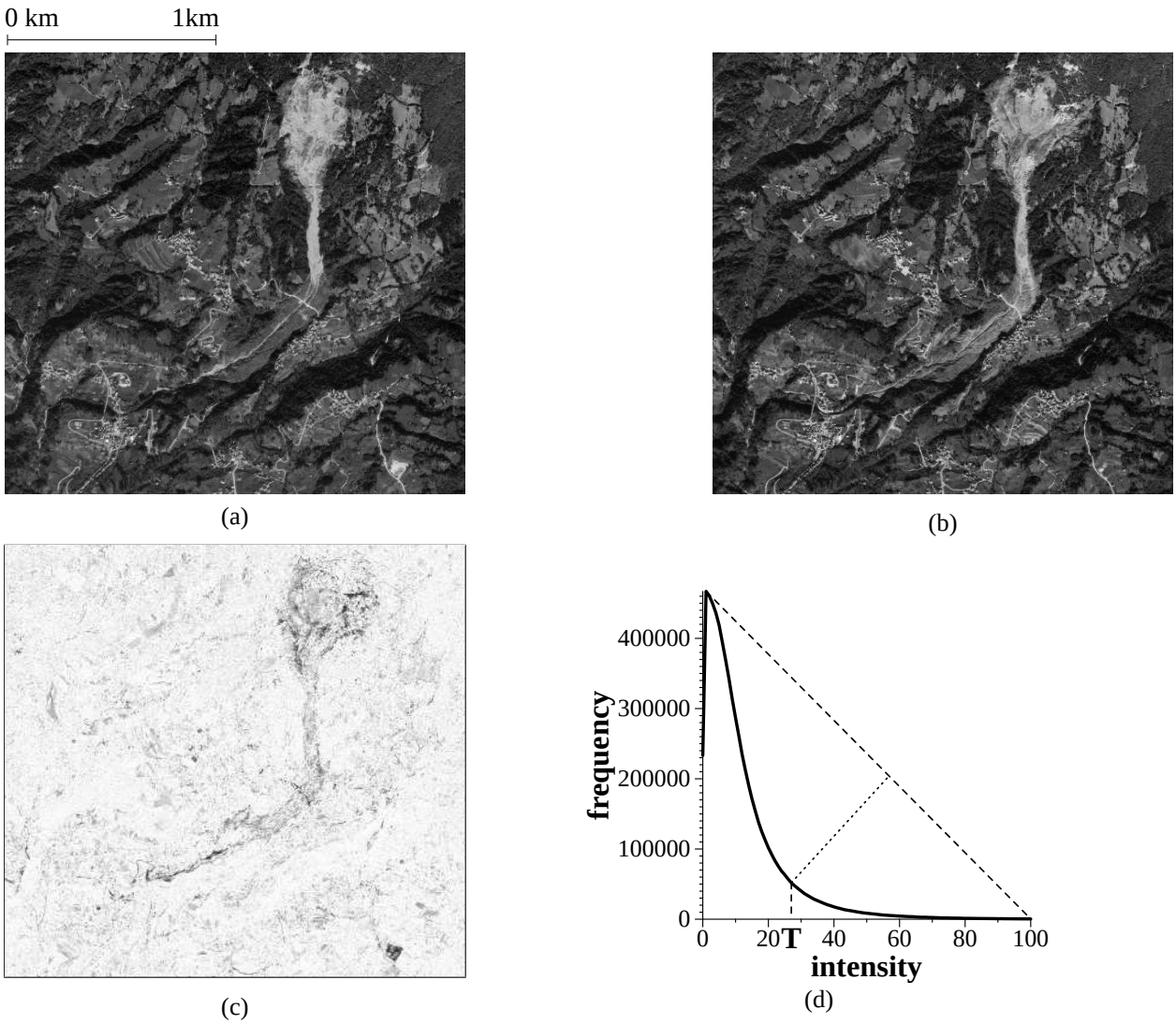

Figure 3: Images of the Tessina landslide area before and after the 1992 reactivation. (a) 28-9-1988, (b) 7-10-1994, (c) inverted difference image (absolute values are taken and black indicates large differences), (d) histogram of difference image, (e) scatter plot of image intensities in corresponding pixels between the 1988 and 1994 images (black indicates high frequency)

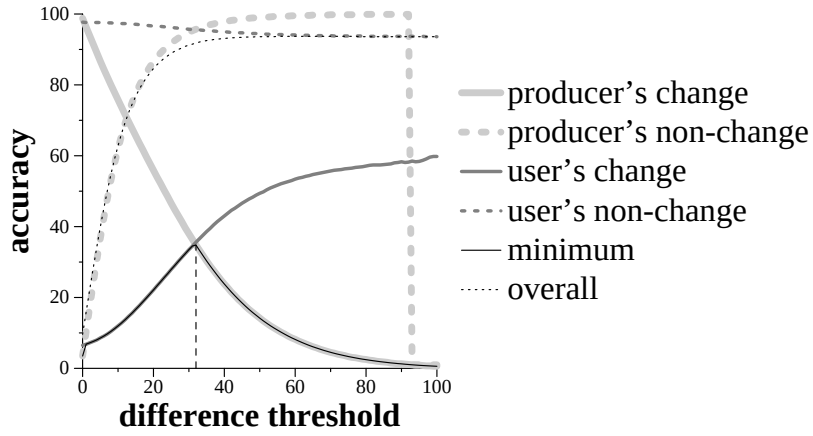

Figure 4: Accuracies of thresholding for all possible thresholds as calculated from the reference data. The peak of the minimum of the four producer/user accuracy values is at the threshold value of 32 as indicated by the dashed line.

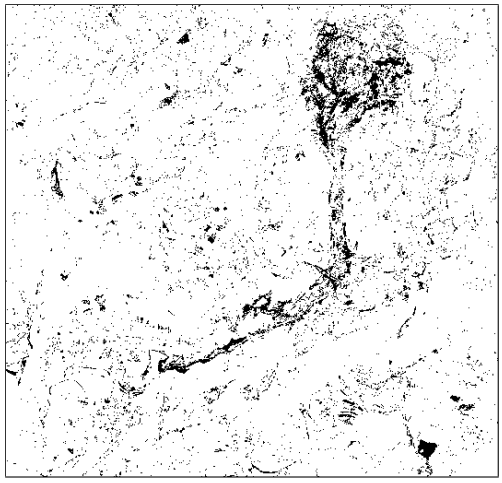

Figure 5: The optimal global thresholding of the difference image according to the minimum of the producer/user accuracy criterion (i.e. the location of the peak in figure 4).

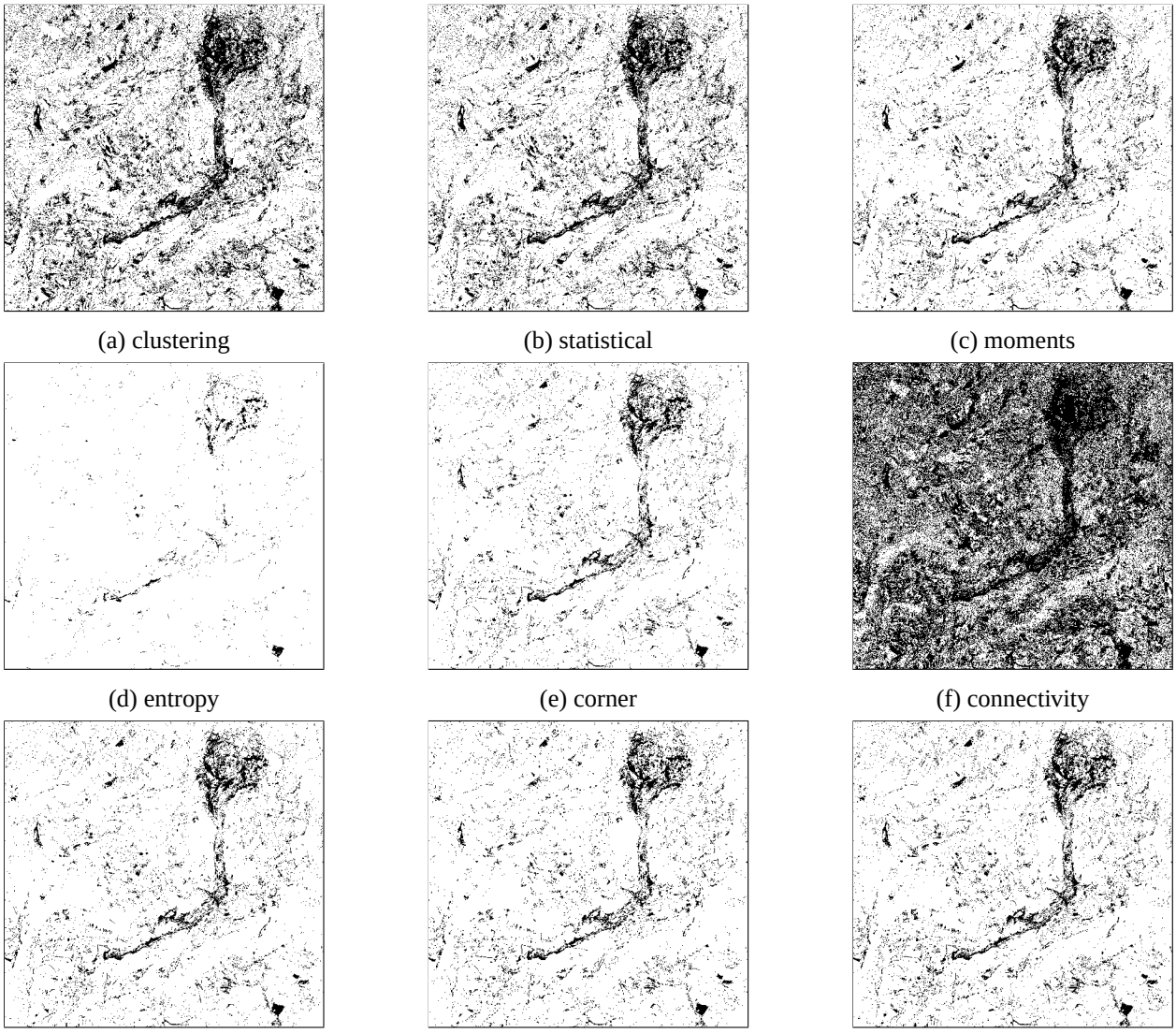

(a) clustering (b) statistical (c) moments

(d) entropy (e) corner (f) connectivity

(g) Poisson (h) LMedS (i) Normal

Figure 6: Binary change map produced by thresholding the difference image using difference methods

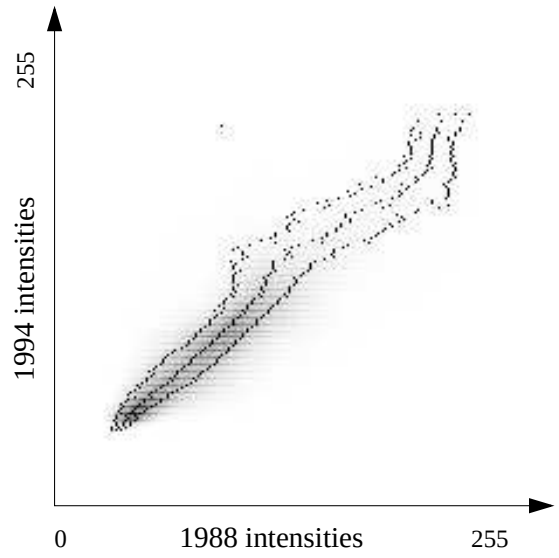

(a) scatter boundaries

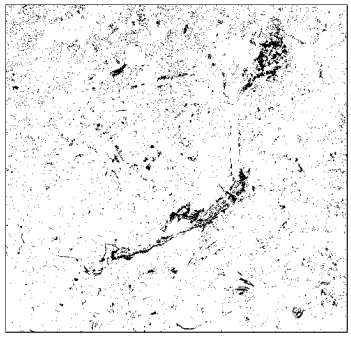

(b) scatter result

Figure 7: Binary change map produced analysing the intensity scatter plot

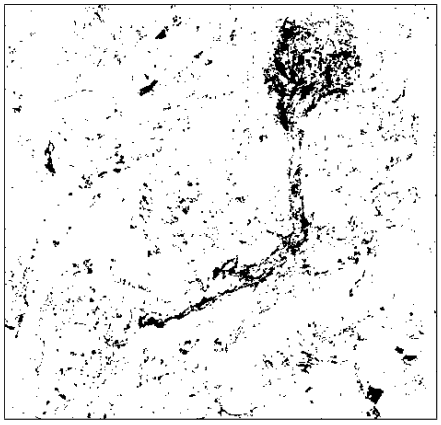

(a) erosion/dilation: 2 iterations

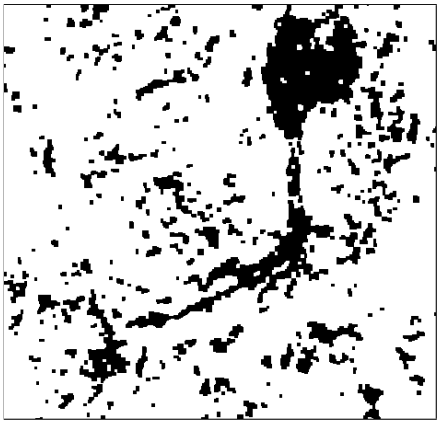

(b) erosion/dilation: 9 iterations

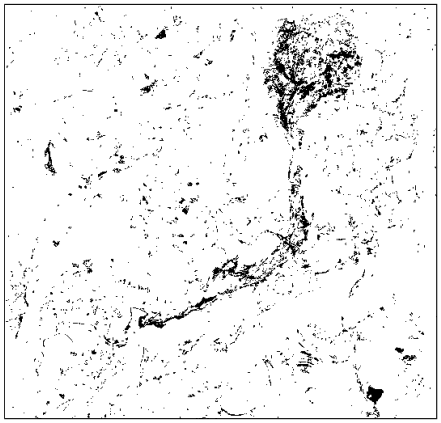

(c) perimeter > 30

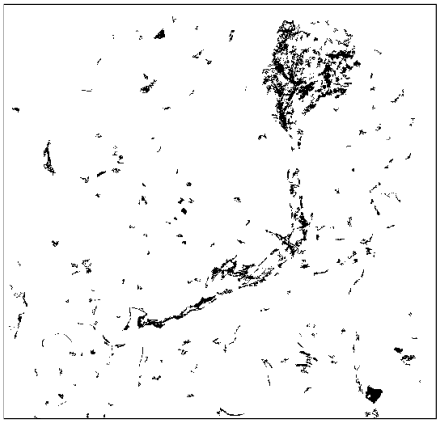

(d) perimeter > 100

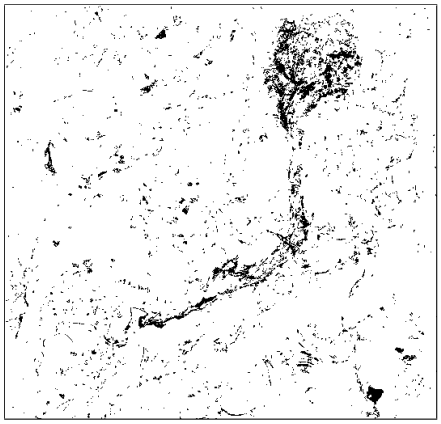

(e) area > 52

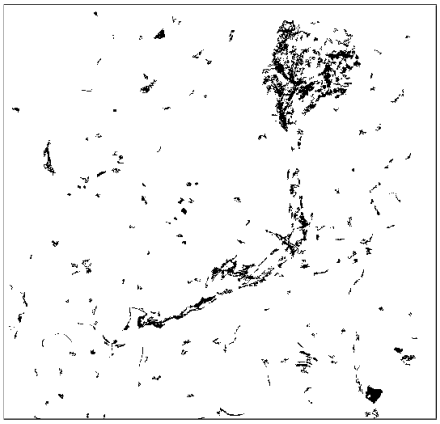

(f) area > 266

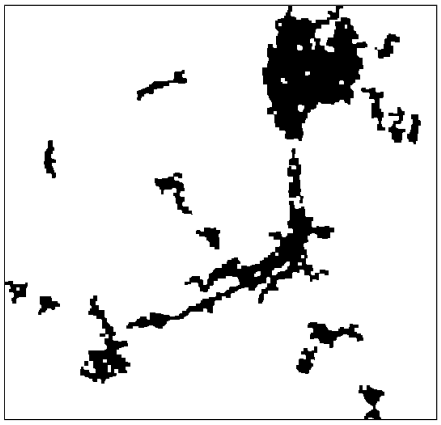

(g) erosion/dilation/area:
9 iterations & area > 10000

Figure 8: Blob filtering of the corner thresholded image using width, perimeter and area properties

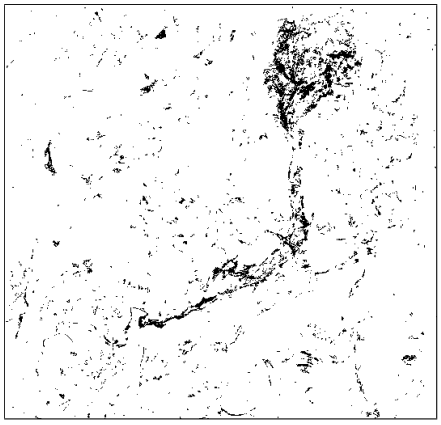

(a) perim. > 30 & rectangularity < 0.6

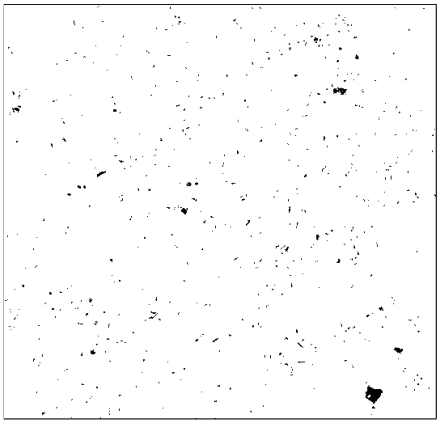

(b) perim. > 30 & rectangularity ≥ 0.6

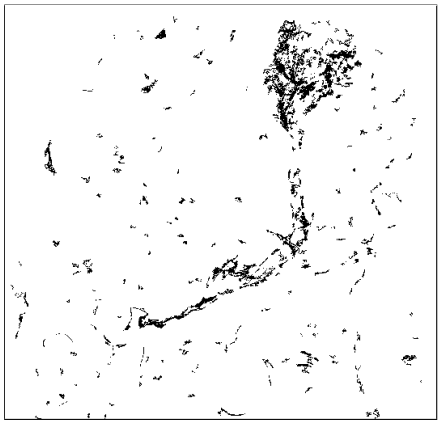

(c) perim. > 100 & rectangularity < 0.6

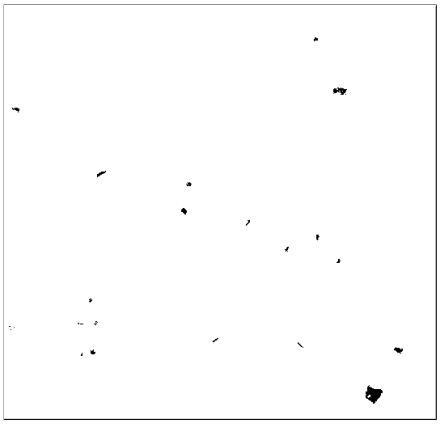

(d) perim. > 100 & rectangularity ≥ 0.6

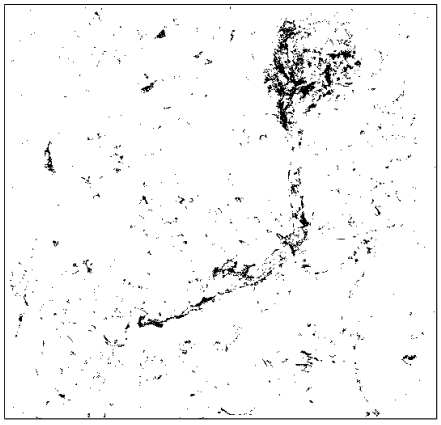

(e) area > 52 & rectangularity < 0.6

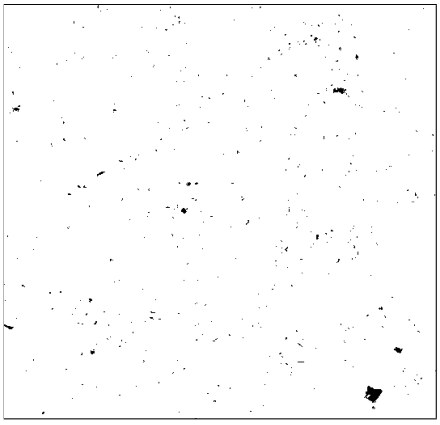

(f) area > 52 & rectangularity ≥ 0.6

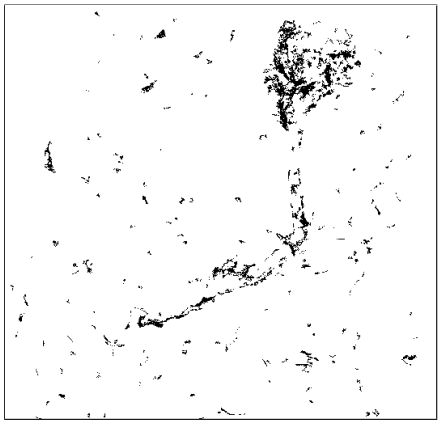

(g) area > 266 & rectangularity < 0.6

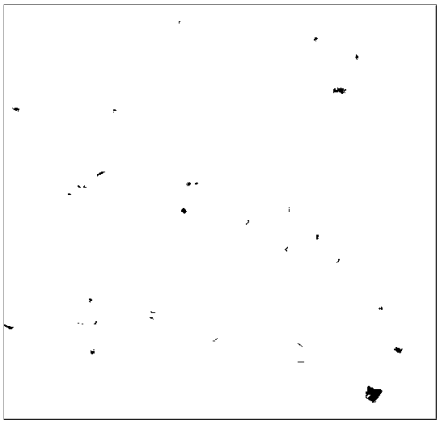

(h) area > 266 & rectangularity ≥ 0.6

Figure 9: Additionally filtering blobs using rectangularity property

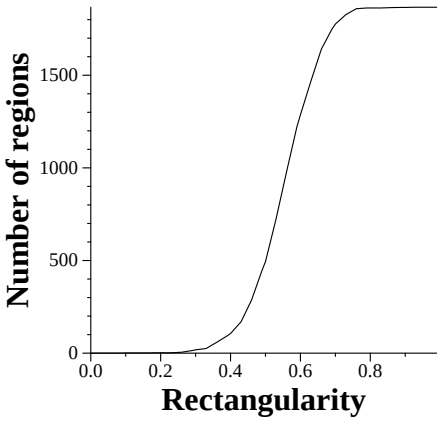

Figure 10: Cumulative number of blobs vs rectangularity threshold

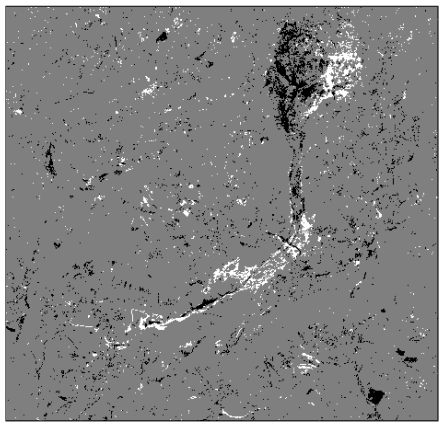

Figure 11: Differentiating between positive and negative intensity changes